Egypt. J. Chem. **Vol. 68**, No. 11 pp. 201 - 215 (2025)

Egyptian Journal of Chemistry

http://ejchem.journals.ekb.eg/

Enhancing Corrosion Resistance of Carbidic and Austempered Carbidic Ductile Iron in Chloride Solutions via Sodium Tungstate Addition

Aliaa Abdelfatah[1], Lamiaa Z. Mohamed[1,*], Hayam A. Aly[2]

[1] Mining, Petroleum and Metallurgical Engineering Department, Faculty of Engineering, Cairo University, Egypt

[2] Central Metallurgical Research and Development Institute (CMRDI), P.O. Box 87, Helwan 11421, Egypt

Abstract

This study investigates the corrosion behavior and surface morphology of carbidic ductile iron (CDI) and carbidic austempered ductile iron (CADI) in 3.5% NaCl, focusing on the effects of heat treatments at 275°C and 375°C and alloying with Nb (0 and 1 wt.%) and Cr (1 and 1.5 wt.%). The corrosion characteristics were evaluated with and without the addition of Na_2WO_4 as an inhibitor (0.1 g and 0.2 g). At 275°C, the 1Cr-Nb alloy exhibited the lowest corrosion rate (CR) of 0.003 mm/y in 3.5% NaCl without inhibition, which further decreased to 0.001 mm/y with the addition of 0.2 g Na_2WO_4. The surface morphology of the corroded alloys reflected their corrosion behavior, revealing evidence of uniform corrosion, localized pitting, and galvanic corrosion. These findings highlight the influence of heat treatment, alloying elements, and inhibition on the corrosion resistance of CDI and CADI in saline environments.

Keywords: Corrosion behavior; Sodium tungstate inhibitor; Carbidic ductile iron; Carbidic austempered ductile iron; Microstructure

1. Introduction

Cast iron has consistently been regarded as a favored material due to its widespread availability, inherent properties, cost-effectiveness, and recyclability. Examples of cast iron types include ductile iron, gray cast iron, and vermicular graphite cast iron [1-3]. Pressure pipes, wind turbines, agricultural machinery, construction, and automobiles, among others, utilize ductile iron, a high-strength material known for its exceptional plastic toughness, fatigue resistance, shock absorption, and tensile strength [4-6]. Ductile iron pipes possess ductile and compressive properties that render them two to three times stronger than gray cast iron pipes [7-9]. Unlike the comprehensive studies on the mechanical properties and wear characteristics of ductile iron in recent decades [10-12], corrosion resistance has historically received less attention [13-16]. Ductile iron manufacture is increasing to meet the market's unquenched need. The metal is durable, enduring, and economical. The mechanical characteristics of nodular cast iron have been the focal point of extensive research. Various alloying elements or the application of suitable heat treatment can achieve this [17-19]. The good strength, ability to harden on the surface, corrosion resistance, high modulus of elasticity, easy casting, and other physical, mechanical, and technological features of ductile iron make it easy for its production to grow quickly. Austempering heat treatment (H.T.) can transform ductile iron into austempered ductile iron (ADI) [20-24]. In terms of the percentage of repair and maintenance expenses attributed to corrosion, ductile iron (DI) components rank highest. Some individuals have hypothesized that the extreme conditions in which these materials operate lead to their eventual degradation in service [25]. ADI has a unique ausferrite microstructure made up of retained austenite that is high in carbon and needle-shaped ferrite [26-29]. Certain iron and aluminum alloys are inferior to materials possessing an ausferrite microstructure. The austempered matrix provides the optimal ratio of ductility to tensile strength among several types of ductile iron. Variations in alloying element concentrations and heat treatment parameters can yield ADI with distinct mechanical properties [30-32]. The proper process involves austenitizing ductile iron at the appropriate temperature for the specified duration, quenching it at the austempering temperature (preferably in a salt bath), and thereafter permitting it to drop to the ambient temperature [33].

Austenitize ductile cast iron commonly procedure at temperatures greater than 850 °C before cooling it in a salt bath kept at 230 to 400 °C to create Austempered Ductile Irons (ADIs). Because carbon and silicon are present in larger proportions in austenite, its transformation behavior during austempering differs from carbon steels [34, 35]. Here, carbon-saturated austenite grows in thin sheets that let ferrite plates form inside the initial austenite grains. As carbon saturation rises, diffusion becomes increasingly limited until it completely stops, thereby halting plate expansion. The stabilization of residual high-carbon austenite is achieved by preventing the production of martensite or cementite and then cooling to normal temperature. Three microstructure components emerge from this process: retained austenite, acicular ferrite, and ausferrite [36-38]. To keep hardness and strength losses to a minimum, low-temperature tempering is a common method [39]. By increasing the possibility of secondary hardening during high-temperature tempering, Cr-cast iron improves the mechanical characteristics of the material even further [40, 41]. However, Ronnie et al. [42] observed a decrease in wear resistance in G350 cast iron as the tempering

*Corresponding author e-mail: lamiaa.zaky@cu.edu.eg ; (Lamiaa Z. Mohamed).

Receive Date: 17 January 2025, Revise Date: 25 February 2025, Accept Date: 23 March 2025

DOI: 10.21608/ejchem.2025.353759.11184

temperature increased, a phenomenon they explained by the development of coarse carbides [43]. Nb also improves toughness, hardness, and wear resistance by changing the temperatures and speeds at which martensite and bainite change into each other [44]. The formation of necessary carbides and nitrides is another way that Cr facilitates austenite crystallization [45, 46]. Research by Chen et al. [47] indicates that nickel alloying significantly influenced the microstructure, toughness, and wear resistance of ADI. Their study primarily focused on the microstructures of graphite and bainite, the bainite transition, and the variables influencing austempering. The Nb enhanced the bainite and pearlite phases by modifying the transition temperature and kinetics. Surface scratching facilitated the incorporation of niobium carbides (NbC) particles into the microstructure. The fact that NbC particles are evenly spread out within eutectic cells suggests that they formed before the eutectic solidified. The results indicated that Nb enhanced the mechanical and microstructural characteristics of the ADI process. When ADI and other graphite cast irons undergo a certain austempering temperature and reduced holding time, needle-like ferrite platelets may develop. Conversely, ferrite exhibits increased coarseness when exposed to elevated austempering temperatures or prolonged holding durations. An additional austempering process can convert carbon-laden austenite into carbide and bainitic ferrite [48]. Carbidic Ductile Iron (CDI) is a type of ductile iron with carbide phases intentionally present in its microstructure. It is specifically designed to offer high hardness and superior wear resistance compared to traditional ductile iron. Its microstructure consists of carbides, typically Cr, Nb, or V carbides, alongside a ferrite or pearlite matrix, which provides some degree of strength, and graphite nodules, which enhance machinability [49]. A subset of ductile cast iron, carbide-austempered ductile iron (CADI), has some unique properties. Carbide inclusions in iron produce an ausferritic matrix that enhances the material's toughness, strength, hardness, and resistance to abrasion. CADI is perfect for usage in the automotive, agricultural, earthmoving, mining, construction, and military industries due to its reduced production complexity and cost-effectiveness [49, 50]. The performance of carbidic ductile iron (CDI) and carbidic austempered ductile iron (CADI) in corrosive environments is of significant concern such as 3.5%NaCl. This study investigates the corrosion behavior of CDI subjected to various heat treatment conditions with additions of Nb (0 and 1 wt.%) and Cr (1 and 1.5 wt.%) in 3.5%NaCl environments with/without inhibitor (Na_2WO_4) (0.1 g and 0.2 g). The austempering temperatures, to transfer the CDI to CADI, are investigated at 275°C and 375°C. The corrosion behavior of the CDI and CADI with different heat treatments using potentiodynamic polarization (PDP) in 3.5% NaCl. Also, the surface morphologies of the corroded CDI and corroded CADI with different heat treatments were investigated.

1. Experimental work

The primary components, comprising steel scrap and Sorel pig iron, are liquefied in a medium-frequency induction furnace. The vortex technique is used to enhance the dispersion of elements or particles in molten metal. It promotes spheroidization and aids in inoculation therapy. All information regarding the alloys' chemical composition can be found in Table 1. Samples undergo austempering at 275 and 375 °C and 375°C for 1.5 h following austenitization at 900 °C for 1 h. The specimens are analyzed via optical microscopy (OM).

Table 1. Chemical compositions of the CDI.

Alloys	Element, wt.%					
	C	Si	Mn	Cr	Nb	Fe
1 % Cr	3.6	2.5	0.2	1.0	--	Bal.
1.5 % Cr	3.6	2.5	0.2	1.5	--	Bal.
1 % Cr-1%Nb	3.6	2.5	0.2	1.0	1.0	Bal.
1.5 % Cr-1%Nb	3.6	2.5	0.2	1.5	1.0	Bal.

2.1 Corrosion Measurements

Potentiodynamic polarization (PDP) experiments were performed on the CDI and CADI samples at room temperature (RT) utilizing a PGZ 100 Potentiostat in conjunction with a three-electrode cell. A saturated calomel electrode (SCE) functioned as one reference electrode, while the other auxiliary electrode was platinum, and the Voltamaster 6 software. Specimens with a surface area of 1 cm² were produced using various SiC grinding papers, from 100 mesh to 1200 mesh. Subsequently, the specimens were polished with 0.3 µm alumina paste. Potentiodynamic polarization (PDP) spanning from -500 mV to 500 mV was employed with a scan rate of 2 mV/s. The specimens (CDI and CADI) were evaluated for electrochemical behavior in a 3.5% NaCl solution, with and without the catalyst sodium tungstate (Na_2WO_4) at concentrations of 0.1 g and 0.2 g, respectively. The electrochemical parameters obtained from the PDP experiment were conductivity (CR), corrosion potential (E_{corr}), and corrosion current density (i_{corr}). The i_{corr} values were derived from Tafel potential diagrams, whereas the corrosion rate (CR) values were computed using Eq. (1) [51-53]:

$$\mathrm{CR\ (mm/y)} = \frac{0.00327 * i_{corr} * \mathrm{Eq.wt}}{D} \qquad (1)$$

The i_{corr} represents the current density (mA/cm^2), Eq. wt. is the equivalent weight (in grams), and D is the specimen density (g/cm^3).

Under varying circumstances of 3.5% NaCl, the surface morphology of the corroded area was studied. The surface appearance, content, and elemental distribution were examined using scanning electron microscopy (SEM).

2. Results and Discussions

3.1. Microstructure Before Corrosion

The optical microstructures of CDI and CADI with different heat treatments were examined. The OM images of CDI alloys are shown in spheroidal graphite and carbides (white regions) in the pearlite matrix in Fig.1. The Cr additive responsible for carbide precipitation in the DI during solidification is called CDI. The OM images of different CADI alloys at 275 °C are provided in Fig. 2. In contrast, the OM images of other CADI alloys at 375 °C are shown in Fig. 3. The OM images of different CADI alloys with various HTs involve graphite spheroids and carbides that are uniformly distributed in the ausferrite matrix. The Cr and Nb additions significantly influence the optical microstructure of CDI and CADI alloys. The Cr promotes the formation of hard carbides, particularly M_7C_3, enhancing wear resistance while refining the microstructure by suppressing the growth of ferrite and pearlite. The Nb, being a strong carbide former, leads to the precipitation of NbC, which acts as nucleation sites, further refining the graphite nodules and primary carbides. In CADI, the austempering process transforms the retained austenite into bainitic ferrite, with Cr and Nb contributing to finer bainitic sheaves and improving phase stability. The combined presence of Cr and Nb enhances the carbide network's homogeneity, leading to a more uniform optical microstructure, with reduced graphite segregation and improved mechanical properties [54].

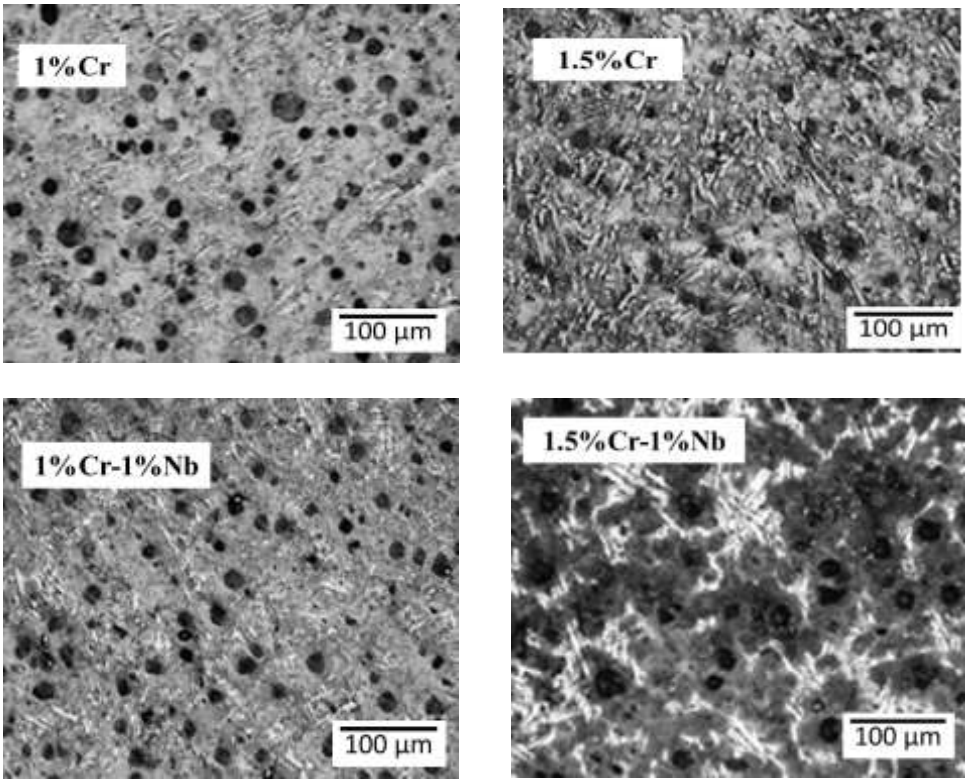

Fig. 1. The OM images of different CDI alloys with different Cr and Nb additions.

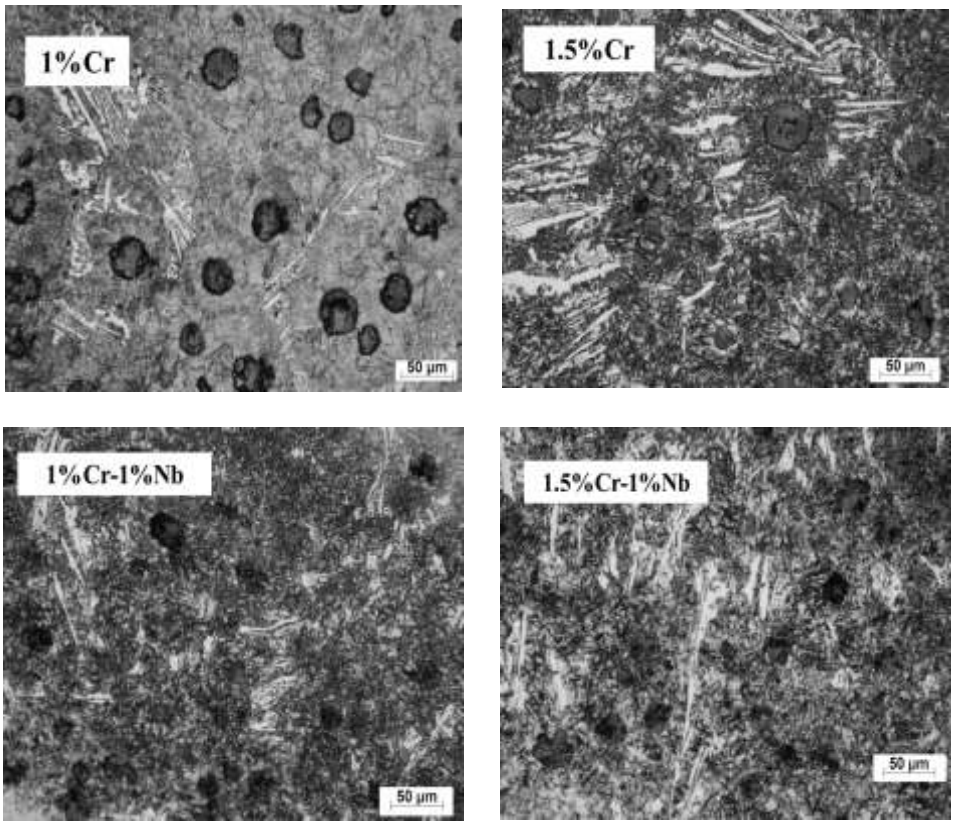

Fig. 2. The OM images of different CADI alloys with heat treatment at 275 °C for different additions of Cr and Nb.

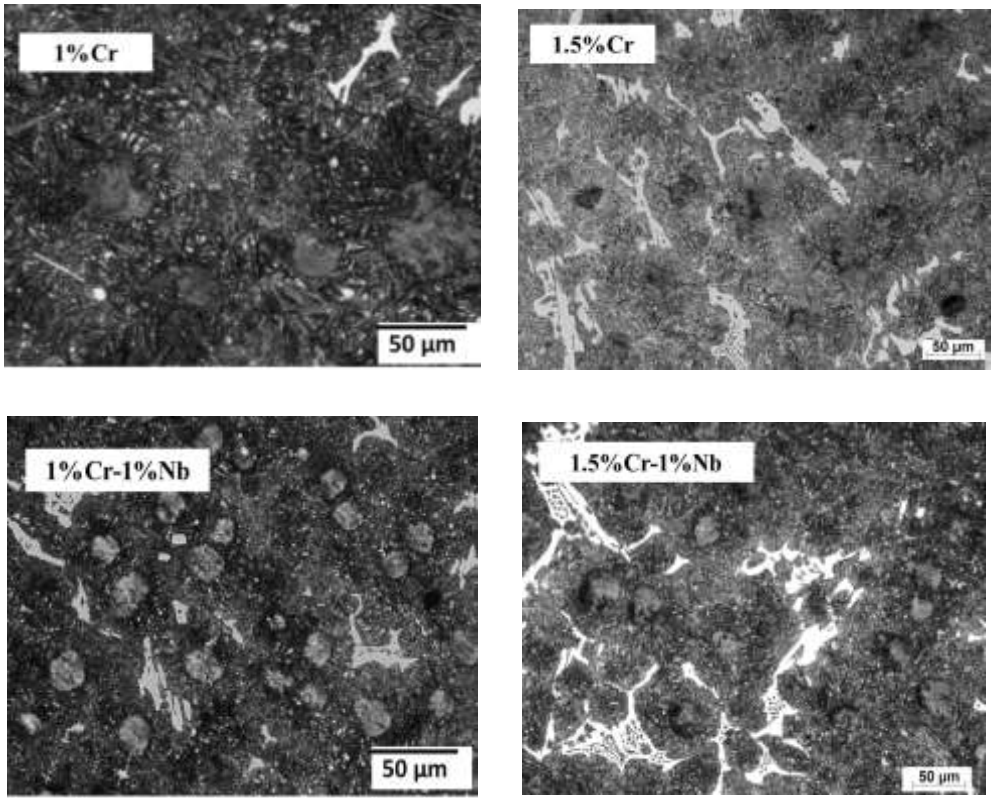

Fig. 3. The OM images of different CADI alloys with heat treatment at 375 °C for different additions of Cr and Nb.

2.2 Corrosion behavior

Potentiodynamic polarization (PDP) curves for CDI and CADI alloys in 3.5% NaCl without inhibitors are presented in Figs. 4, 5, and 6, with the corresponding electrochemical parameters summarized in Table 2. Fig. 4 shows the PDP plots of CDI alloys, while Figs 5 and 6 display the PDP curves of CADI at austempering temperatures of 275°C and 375°C, respectively. According to Table 2, the lowest CR value in CDI alloy exposed to 3.5% NaCl is observed for the 1.5Cr-Nb sample (0.252 mm/y), whereas the highest CR is recorded for the 1Cr sample (0.405 mm/y). This improved corrosion resistance is attributed to the formation of a protective chromium oxide layer on the surface. However, after heat treatment at 275°C and 375°C, Cr and Nb promote carbide formation, which results in increased CR values. The formation of niobium carbides reduces the potential for chromium carbide formation, thereby enhancing corrosion resistance. At 275°C, the 1Cr-Nb alloy shows the lowest CR (0.003 mm/y), while the 1.5Cr alloy exhibits the highest CR (0.450 mm/y). Increasing the heat treatment temperature to 375°C promotes the formation of more carbides, further diminishing corrosion resistance. At 375°C, the 1Cr-Nb alloy again demonstrates the lowest CR (0.016 mm/y), whereas the 1.5Cr alloy reaches the highest CR (0.863 mm/y).

The corrosion resistance of CADI samples subjected to elevated austempering temperatures in NaCl solutions is improved. Localized corrosion phenomena, such as pitting, are less probable when a more homogeneous ausferritic structure develops. The alloy surface exhibits enhanced protection against chloride-induced corrosion due to the increased stability of the passive film. Conversely, CADI treated to lower temperatures exhibits a suboptimal phase distribution and diminished passive film formation, rendering it more susceptible to corrosion. Austempering generates bainitic ferrite and high-carbon-retained austenite by diminishing current density and augmenting potential, hence enhancing corrosion resistance to CADI [55]. The Nb enhances cast iron's tensile strength, hardness, and wear resistance while maintaining its toughness. The incorporation of nickel into cast iron alters its microstructure, resulting in a refinement of the graphite and eutectic structures. The corrosion resistance of some cast irons correlates with the nickel content. Niobium carbides precipitate from liquids upon addition [56].

Table 2. The electrochemical parameters from Tafel of different CDI and CADI alloys without inhibitor in 3.5%NaCl.

Alloys		E_{corr} mV	I_{corr} µA/cm^2	CR, mm/y
CDI	1 Cr	-883.4	0.059	0.405
	1.5 Cr	-888.7	0.054	0.368
	1 Cr-Nb	-657.2	0.056	0.381
	1.5 Cr-Nb	-708.7	0.037	0.252
CADI (275°C)	1 Cr	-689.8	0.023	0.158
	1.5 Cr	-854.0	0.066	0.450
	1 Cr-Nb	-778.3	0.005	0.003
	1.5 Cr-Nb	-636.6	0.057	0.071
CADI (375°C)	1 Cr	-771.4	0.109	0.742
	1.5 Cr	-755.3	0.126	0.863
	1 Cr-Nb	-637.0	0.002	0.016
	1.5 Cr-Nb	-681.8	0.008	0.057

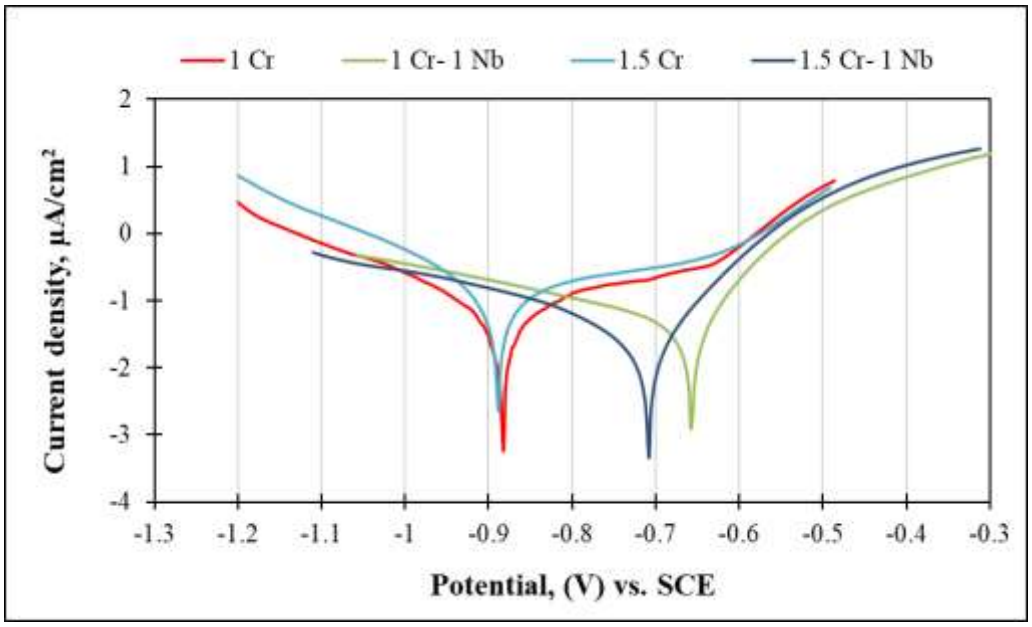

Fig. 4. The PDP plots of the CDI alloys with different additions of Cr and Nb at RT.

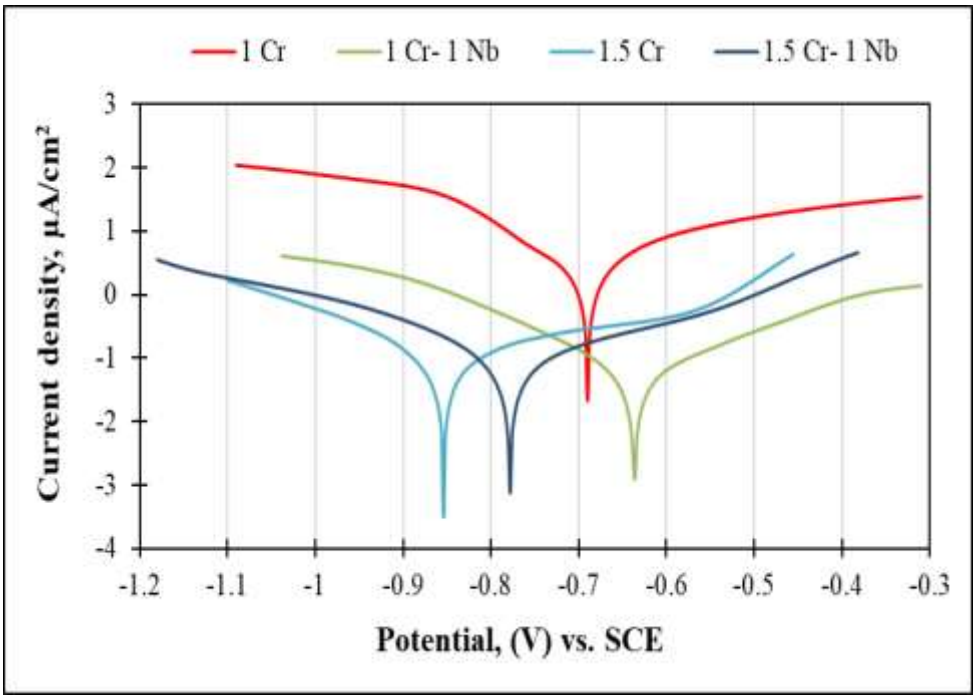

Fig. 5. The PDP plots of the CADI with heat treatment at 275 °C with different additions of Cr and Nb at RT.

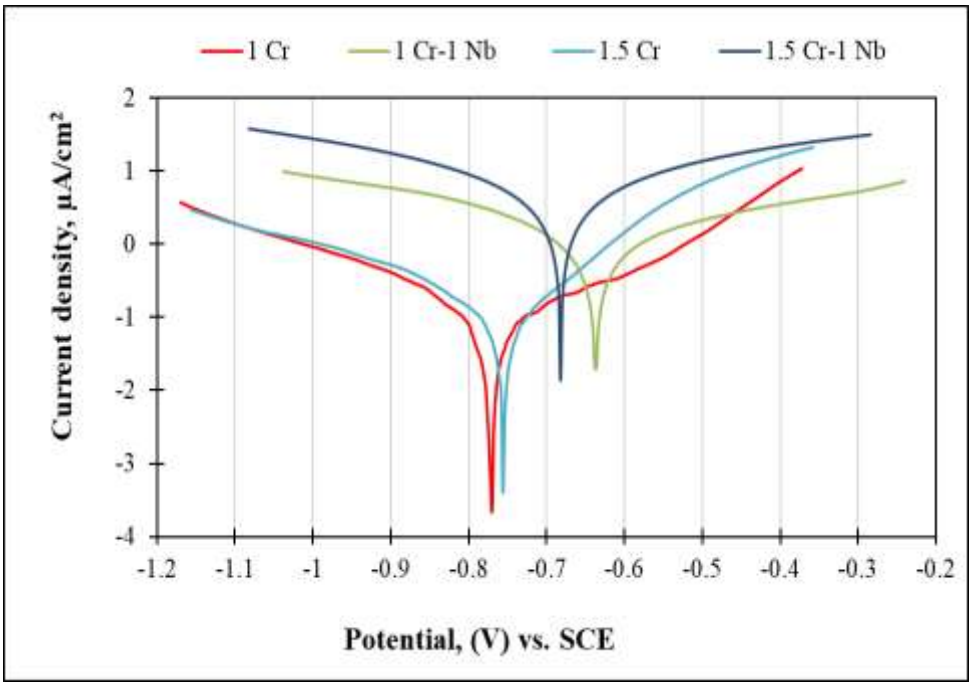

Fig. 6. The PDP plots of the CADI with heat treatment at 375 °C with different additions of Cr and Nb at RT.

The PDP curves for various conditions of CDI and CADI in 3.5% NaCl with 0.1 g Na_2WO_4 are shown in Figs 7, 8, and 9, with the corresponding electrochemical parameters summarized in Table 3. Fig. 7 presents the PDP plots for CDI alloys, while Figs 8 and 9 display the PDP curves for CADI at austempering temperatures of 275°C and 375°C, respectively. The corrosion behavior follows a similar trend to that observed without the inhibitor for both CDI and CADI alloys. In 3.5% NaCl with 0.1 g Na_2WO_4, the lowest CR value for CDI is recorded for the 1.5Cr-Nb alloy (2.09 mm/y), while the highest CR is observed for the 1Cr alloy (8.37 mm/y). After heat treatment at 275°C, the 1Cr-Nb alloy exhibits the lowest CR (0.038 mm/y), whereas the highest CR is found for the 1.5Cr alloy (1.321 mm/y). At 375°C, the 1Cr-Nb alloy again shows the lowest CR (0.149 mm/y), with the highest CR recorded for the 1.5Cr alloy (2.626 mm/y).

Table 3. The electrochemical parameters from the Tafel plots of different CDI and CADI alloys in 3.5%NaCl with 0.1 g Na_2WO_4.

Alloys		E_{corr} , mV	I_{corr} , µA/cm^2	CR, mm/y
CDI	1 Cr	-866.8	1.226	8.37
	1.5 Cr	-846.0	0.392	2.58
	1 Cr-Nb	-916.3	0.516	3.52
	1.5 Cr-Nb	-767.6	0.306	2.09
CADI (275°C)	1 Cr	-814.7	0.065	0.440
	1.5 Cr	-743.9	0.194	1.321
	1 Cr-Nb	-522.9	0.005	0.038
	1.5 Cr-Nb	-755.6	0.056	0.386
CADI (375°C)	1 Cr	-782.8	0.155	1.061
	1.5 Cr	-738.2	0.385	2.626
	1 Cr-Nb	-731.1	0.022	0.149
	1.5 Cr-Nb	-773.2	0.142	0.969

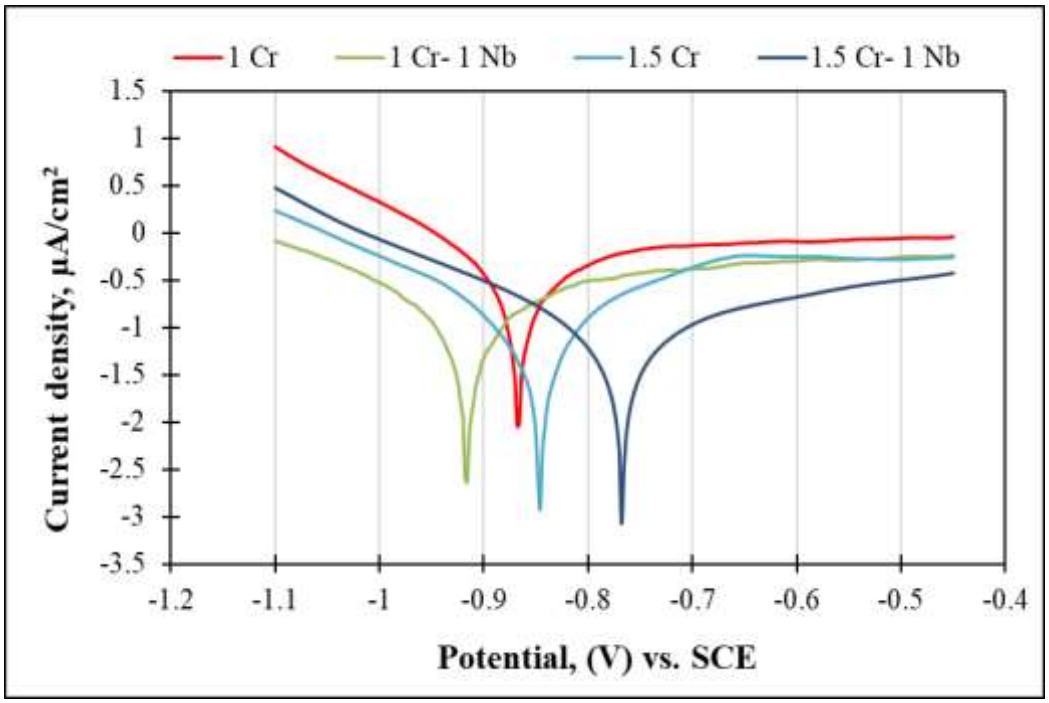

Fig. 7. The PDP plots of the CDI alloys with different additions of Cr and Nb with 0.1 g Na_2WO_4 at RT.

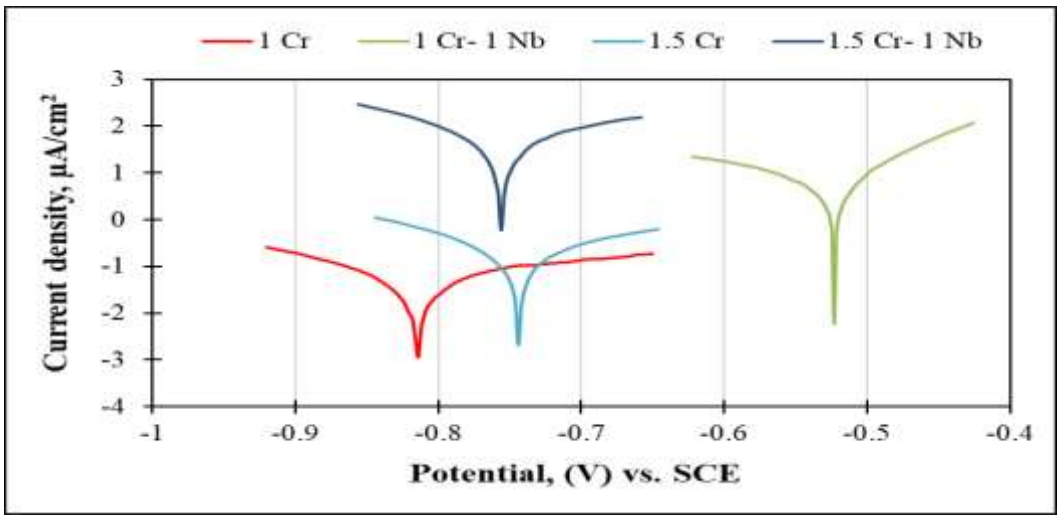

Fig. 8. The PDP plots of the CADI with heat treatment at 275 °C with different additions of Cr and Nb with 0.1 g Na_2WO_4 at RT.

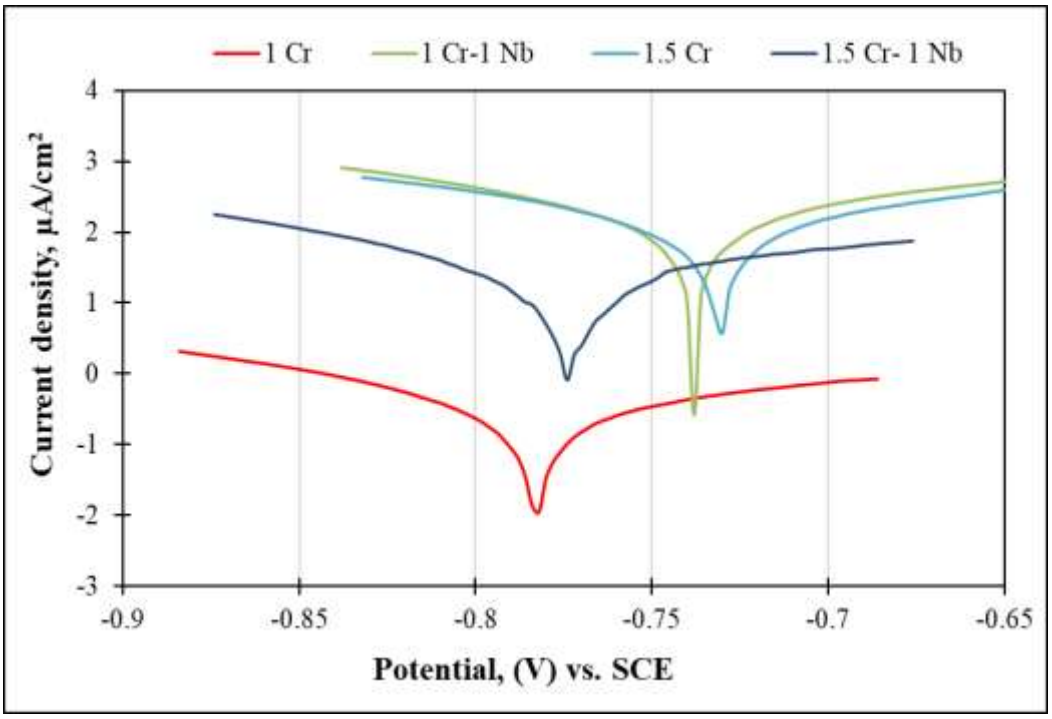

Fig. 9. The PDP plots of the CADI with heat treatment at 375 °C with different additions of Cr and Nb with 0.1 g Na_2WO_4 at RT.

The PDP curves of different CDI alloys in 3.5%NaCl with 0.2 g Na_2WO_4 are presented in Figs. 10, 11, and 12. The electrochemical parameters are revealed in Table 4. Fig. 10 represents the PDP plots of the CDI alloys. Figs 11 and 12 show the PDP curves of CADI with the austempering temperatures 275°C and 375°C, respectively. In 3.5% NaCl with 0.2g Na_2WO_4, the lowest CR value for CDI is recorded for the 1.5Cr-Nb alloy (0.028 mm/y), while the highest CR is observed for the 1Cr alloy (0.236 mm/y). After heat treatment at 275°C, the 1Cr-Nb alloy exhibits the lowest CR (0.001 mm/y), whereas the highest CR is found for the 1.5Cr alloy (0.016 mm/y). At 375°C, the 1Cr-Nb alloy again shows the lowest CR (0.617 mm/y), with the highest CR recorded for the 1.5Cr alloy (3.128 mm/y). Sodium tungstate promotes the formation of an oxide layer, which passivates the alloy surface and prevents further interaction with corrosive chloride ions [57]. In alloys containing elements like Cr and Nb, tungstate ions can complement the formation of stable oxide or carbide layers, improving the alloy's overall corrosion resistance. The presence of Na_2WO_4 significantly decreases the CR. Thus, the addition of 0.2g Na_2WO_4 led to a decrease in the CR values than those without inhibition [58].

Table 4. The electrochemical parameters from the Tafel plots of different CDI and CADI alloys with 0.2 g Na_2WO_4.

Alloys		E_{corr} , mV	I_{corr} , µA/cm²	CR, mm/y
CDI	1 Cr	-742.8	0.034	0.236
	1.5 Cr	-635.3	0.007	0.050
	1 Cr-Nb	-639.9	0.009	0.061
	1.5 Cr-Nb	-626.5	0.004	0.028
CADI (275°C)	1 Cr	-523.1	0.001	0.010
	1.5 Cr	-625.0	0.002	0.016
	1 Cr-Nb	-545.7	0.0001	0.001
	1.5 Cr-Nb	-539.2	0.0007	0.005
CADI (375°C)	1 Cr	-750.4	0.361	2.466
	1.5 Cr	-683.1	0.458	3.128
	1 Cr-Nb	-708.0	0.098	0.617
	1.5 Cr-Nb	-670.7	0.315	2.152

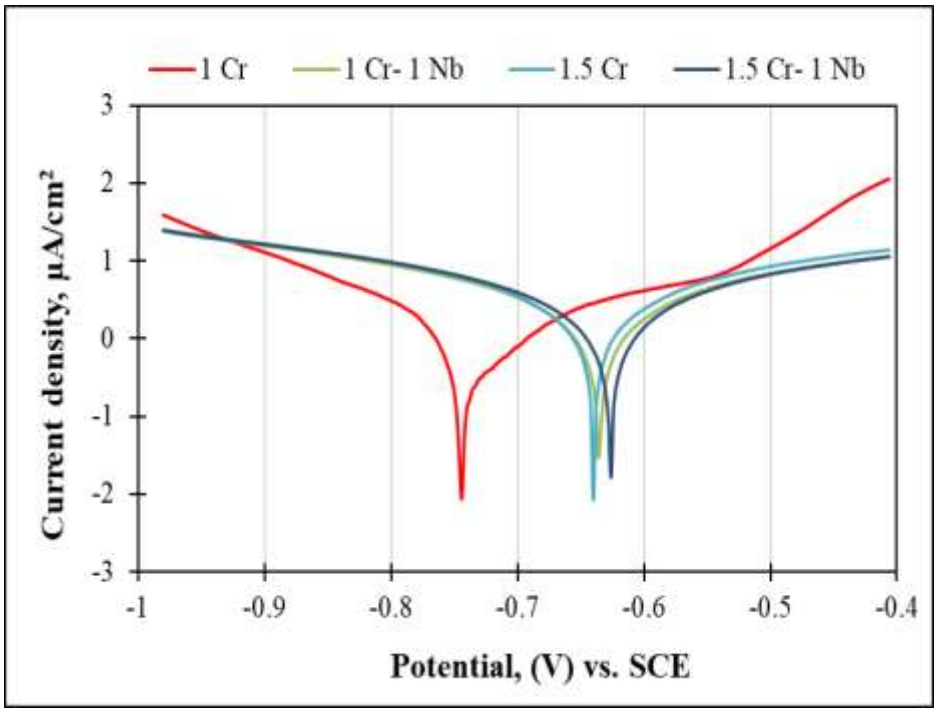

Fig. 10. The PDP plots of the CDI alloys with different additions of Cr and Nb with 0.2 g Na_2WO_4 at RT.

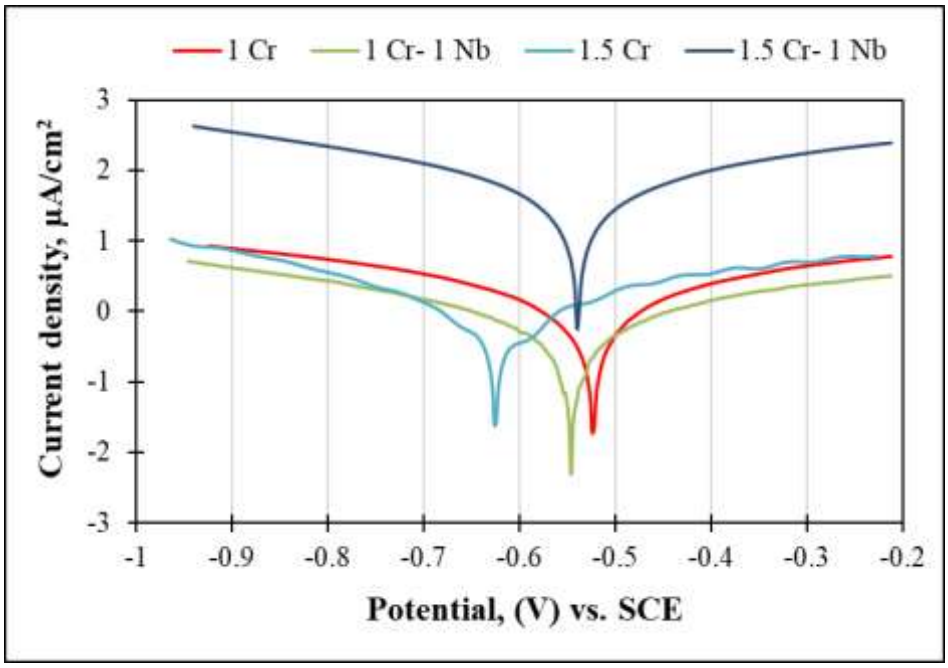

Fig. 11. The PDP plots of the CADI with heat treatment at 275 °C with different additions of Cr and Nb with 0.2 g Na_2WO_4 at RT.

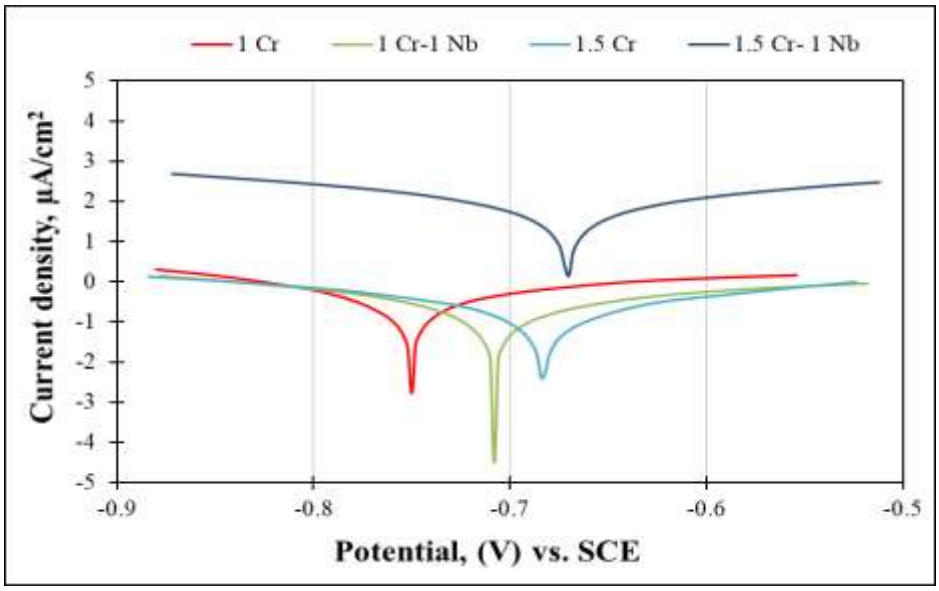

Fig. 12. The PDP plots of the CADI with heat treatment at 375 °C with different additions of Cr and Nb with 0.2 g Na_2WO_4 at RT.

In NaCl solutions, chloride ions are highly aggressive towards alloys. These ions can disrupt the passive oxide film on the surface of CDI and CADI, leading to localized corrosion reactions. The general reaction of iron with chloride ions in an aqueous environment can be represented as:

$$Fe + 2Cl^- + 2H_2O \rightarrow FeCl_2 + 2OH^- \quad (2)$$

Pitting corrosion is a localized form of corrosion where small pits or holes develop on the alloy surface. This is particularly pronounced in CDI and CADI samples with inadequate heat treatment. The chloride ions penetrate the passive layer, leading to:

$$Fe + 2Cl^- \rightarrow FeCl_2 \quad (3)$$

The formation of iron chloride in the pits accelerates the degradation process.
General corrosion in CDI and CADI alloys occurs when the overall passive layer is compromised. This can be described by the general oxidation reaction of iron:

$$Fe + O_2 + 2H_2O \rightarrow Fe(OH)_2 \quad (4)$$

Chloride ions interfere with the corrosion process, perhaps resulting in elevated CR values in NaCl compared to other solutions. Initially, sufficient oxygen can permeate the material, facilitating the movement of Cl^- ions toward the surface defects in CDI and CADI alloys [1]. The CR of the submerged specimen decreases linearly as the tungstate concentration increases. As little as 0.2 g of tungstate is added, tungstate ions form a hydrated oxide film that acts as a passivation layer to stop anodic dissolution. At high concentrations in tap water, tungstate adsorption on the top layer of the hydrated oxide coating breaks down. This action obstructs the migration of Fe^{3+} ions from the alloy surface and precludes harmful ions from infiltrating the matrix [59].

3.3 Microstructure

The CDI and CADI have different surface morphologies in 3.5% NaCl because of microstructural alterations induced by heat treatments and alloying processes. Although CDI has a moderate hardness, its surface is sensitive because of the arrangement of carbide ions within its pearlitic or ferritic matrix. These carbides may be effective in inhibiting localized corrosion by reacting with a sodium tungstate and 3.5% NaCl solution. Nevertheless, stress induced by corrosion may still lead to the formation of microcracks within the structure. Ausferrite, a unique microstructure formed during austempering, is found in CADI. This ausferritic matrix preserves and enhances the abrasion resistance of the carbides while also improving toughness. Sodium tungstate enhances its corrosion resistance relative to CDI by stabilizing and improving its microstructure. This is accomplished by minimizing the formation of cracks and localized corrosion points. Tungstate ions enhance performance in saline settings through two mechanisms. Initially, they apply protective coatings to the iron matrix, which inhibits pitting [52, 60].

Figs. 13 and 14 illustrate the microstructures under different conditions. In CDI, graphite particles of varying sizes are uniformly distributed. While uniform corrosion and galvanic corrosion are significant concerns for both CDI and CADI, pitting corrosion also presents a considerable challenge. Localized corrosion can occur if chloride ions penetrate the passive layer. The microstructure of CDI and CADI, characterized by a stable ausferritic structure, exhibits greater uniformity and improved integrity of the passive film. As a result, the likelihood of pitting corrosion is reduced. Two critical factors influencing overall CR values are the quality of the passive film and the homogeneity of the microstructure. The enhanced microstructure facilitates the maintenance of a stable passive film, thereby decreasing the uniform corrosion and extending the material's service life. However, the formation of carbides at temperatures of 275 °C and 375 °C can exacerbate galvanic corrosion.

Fig. 13 illustrates the surface morphology of the corroded CADI alloys subjected to different heat treatments (275 °C and 375 °C) in 3.5% NaCl without an inhibitor. Pitting corrosion is evident in all images, with a more pronounced occurrence at 375 °C compared to 275 °C, consistent with the CR values presented in Table 2. Fig. 14 displays the surface morphology of the CDI and CADI alloys in 3.5% NaCl with 0.2 g Na_2WO_4. In this figure, both pitting and galvanic corrosion are observed alongside uniform corrosion. The 1.5Cr-Nb alloy in CDI shows the lowest level of pitting corrosion, while the CADI 1Cr-Nb alloy demonstrates the least pitting and galvanic corrosion across both heat treatments, aligning with the CR values shown in Table 4. Tungstate mitigates corrosion by forming a passivation layer as a hydrated oxide film [59].

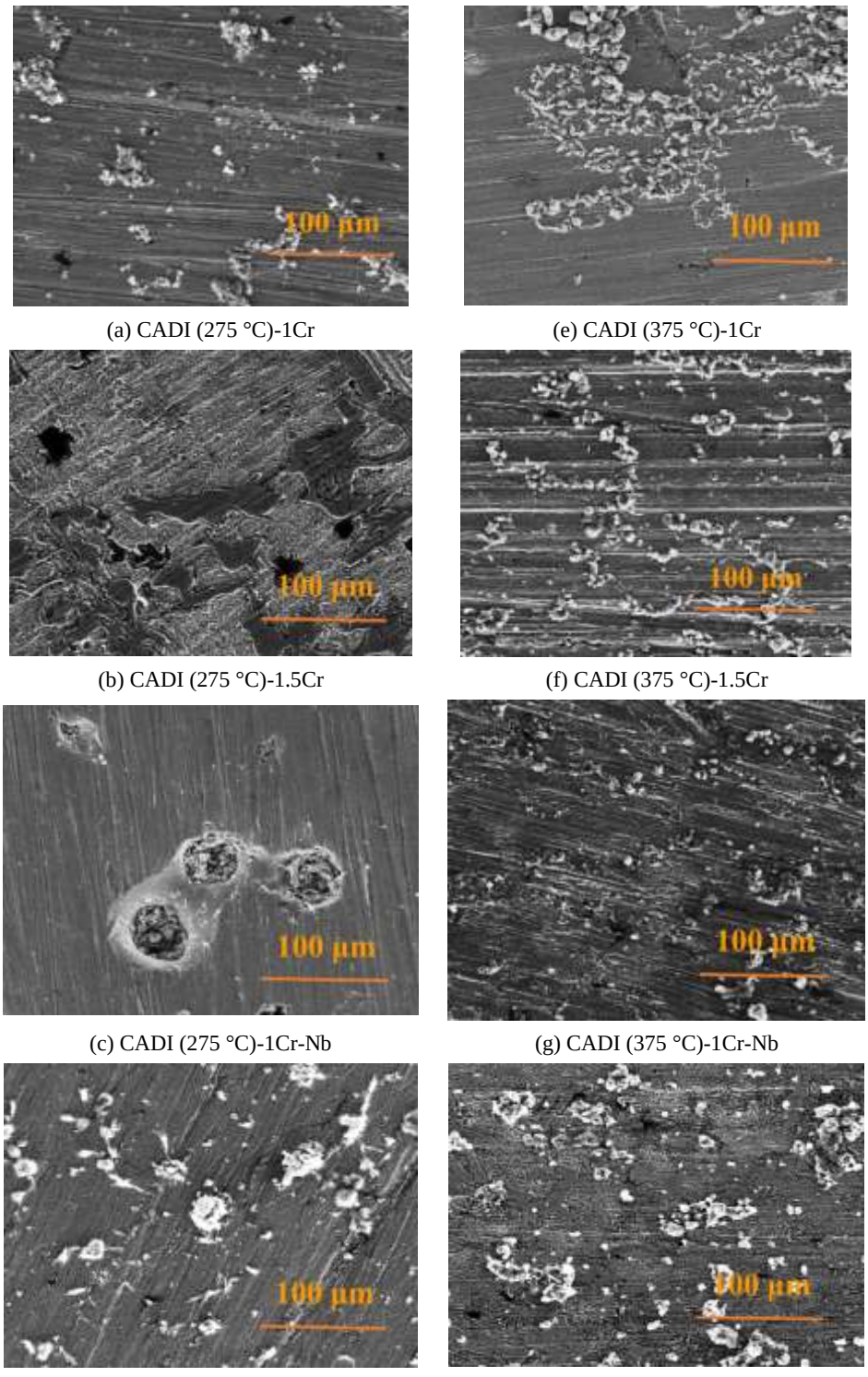

(a) CADI (275 °C)-1Cr (e) CADI (375 °C)-1Cr

(b) CADI (275 °C)-1.5Cr (f) CADI (375 °C)-1.5Cr

(c) CADI (275 °C)-1Cr-Nb (g) CADI (375 °C)-1Cr-Nb

(d) CADI (275 °C)-1.5Cr-Nb (h) CADI (375 °C)-1.5Cr-Nb

Fig. 13. The SEM morphologies of different corroded CADI alloys in 3.5% NaCl without inhibitor.

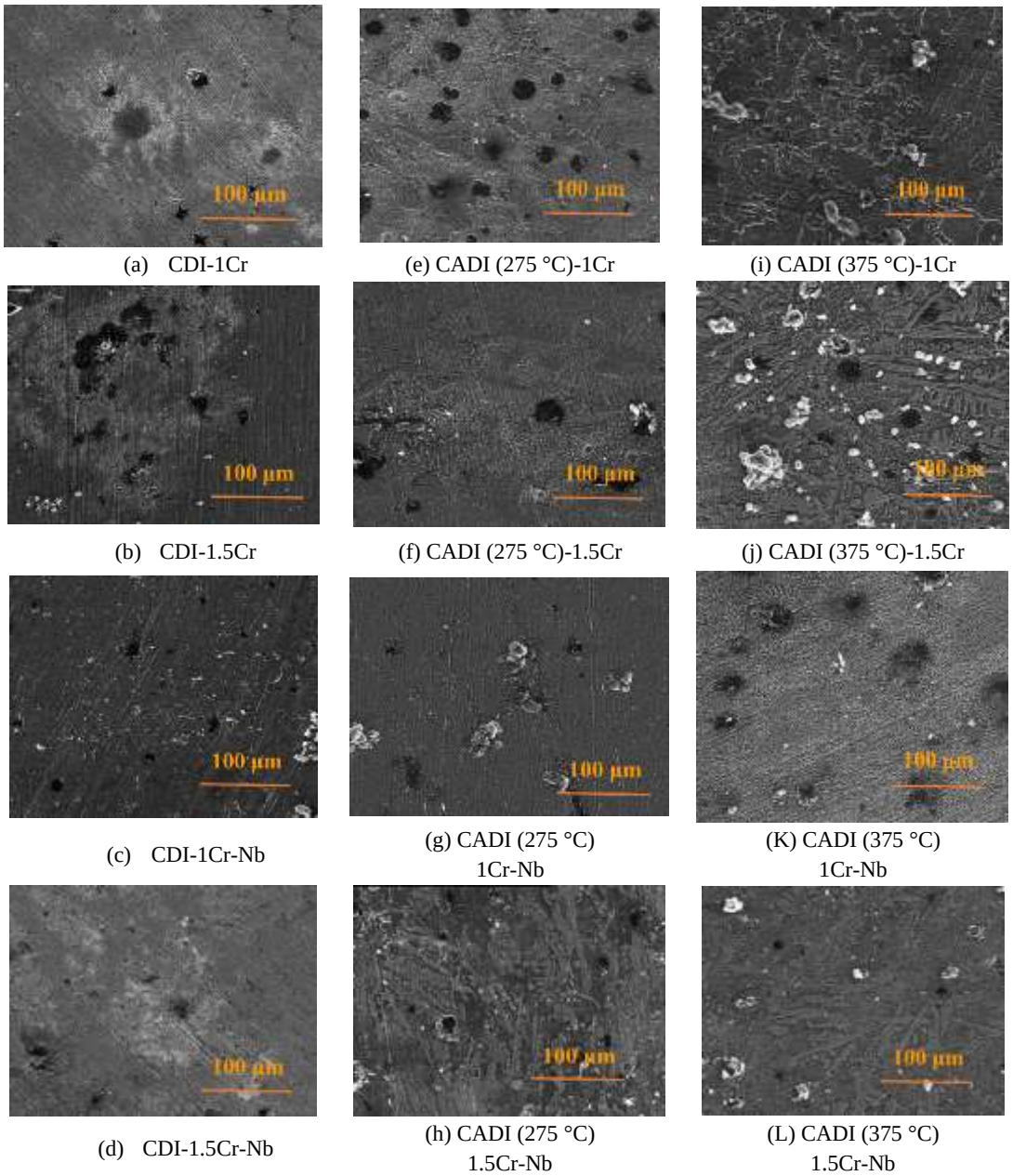

Fig. 14. The SEM morphologies of different corroded CDI and CADI alloys in 3.5% NaCl with 0.2g Na_2WO_4.

Conclusions

This study investigated the corrosion behavior of carbidic ductile iron (CDI) and carbidic austempered ductile iron (CADI) in 3.5% NaCl, both with and without Na_2WO_4 as an inhibitor. The key findings are summarized as follows:

1. In 3.5% NaCl, the 1.5Cr-Nb sample of the CDI alloy demonstrated the lowest corrosion rate (CR) at 0.252 mm/y, while the 1Cr sample exhibited the highest CR at 0.405 mm/y. With the addition of 0.2 g of Na_2WO_4, the CR of the 1.5Cr-Nb alloy further decreased to 0.028 mm/y, whereas the 1Cr alloy showed the highest CR of 0.236 mm/y. This improvement is attributed to the formation of protective oxide layers that reduce further degradation.
2. At 275°C, the 1Cr-Nb alloy recorded the lowest CR of 0.003 mm/y in 3.5% NaCl without inhibition. Adding 0.2 g of Na_2WO_4 reduced the CR to 0.001 mm/y. At 375°C, the 1Cr-Nb alloy again showed the lowest CR of 0.016 mm/y, while the 1.5Cr alloy exhibited the highest CR of 0.863 mm/y. When 0.2 g of Na_2WO_4 was added, the 1Cr-Nb alloy maintained the lowest CR at 0.617 mm/y, and the 1.5Cr alloy reached the highest CR at 3.128 mm/y. The higher CR with increased Cr content is attributed to carbide formation, while Nb addition helped mitigate degradation. Effective corrosion inhibition of ductile cast iron required a high concentration of tungstate.

3. The surface morphology of the corroded alloys aligned with their corrosion behavior, showing uniform corrosion, localized pitting, and galvanic corrosion. Galvanic corrosion was more pronounced with increased carbide formation at both 275°C and 375°C.

Conflict of interest

The authors declare that they have no conflicts of interest.

Data availability statement

My manuscript has no associated data.

References

[1]. T. Chen, B. Wang, L. Sun, C. Liu, X. Cheng, X. Li, The coupling mechanism of shrinkage defects and graphite on the corrosion resistance of ductile iron, Corrosion Science 227 (2024) 111798.

[2]. O.J. Akinribide, O.D. Ogundare, O.M. Oluwafemi, K. Ebisike, A.K. Nageri, S. O. Akinwamide, F. Gamaoun, P.A. Olubambi, A review on heat treatment of cast iron: phase evolution and mechanical characterization, Materials 15 (2022) 7109.

[3]. K. Ruangchai, R. Tongsri, J.T.H. Pearce, T. Chairuangsri, S. Nusen, H. Kurata, M. Haruta, T. Kiyomura, A. Yamaguchi, A. Wiengmoon, Electron microscopy of carbides in annealed 28 wt% Cr - 1 wt% (Mo/W) cast irons, Mater. Charact. 198 (2023), 112723.

[4]. A. Ebel, O. Marsan, J. Lacaze, B. Malard, Cyclic oxidation of high-silicon spheroidal graphite iron, Corros. Sci. 192 (2021), 109854.

[5]. T. Wigger, T. Andriollo, C. Xu, S.J. Clark, Z. Gong, R.C. Atwood, J.H. Hattel, N. S. Tiedje, P.D. Lee, M.A. Azeem, In situ synchrotron investigation of degenerate graphite nodule evolution in ductile cast iron, Acta Mater. 221 (2021), 117367.

[6]. H. Wu, H. Peng, Y. Liu, H. Tu, J. Wang, X. Su, Effect of selective pre-oxidation on the growth and corrosion resistance of hot-dip zinc coating of nodular cast iron, Corros. Sci. 186 (2021), 109463.

[7]. P.-M. Geffroy, M. Lakehal, J. Go˜ni, E. Beaugnon, J.-F. Silvain, Thermal and mechanical behaviour of grey cast iron and ductile iron castings using magnetic molding and lost foam processes, J. Mater. Process. Technol. 209 (2009) 4103–4111.

[8]. K.-F. Nilsson, V. Vok´al, Analysis of ductile cast iron tensile tests to relate ductility variation to casting defects and material microstructure, Mater. Sci. Eng.: A 502 (2009) 54–63.

[9]. X.Y. Teng, J.C. Pang, F. Liu, C.L. Zou, C. Gao, S.X. Li, Z.F. Zhang, Fatigue strength optimization of gray cast iron processed by different austempering temperatures, Int. J. Fatigue 175 (2023), 107831.

[10]. L. Collini, A. Pirondi, Microstructural, multilevel simulation of notch effect in ferritic ductile cast iron under low cycle fatigue, Int. J. Fatigue 162 (2022), 106993.

[11]. C. Liu, Y. Du, X. Wang, Z. Hu, P. Li, K. Wang, D. Liu, B. Jiang, Mechanical and tribological behavior of dual-phase ductile iron with different martensite amounts, J. Mater. Res. Technol. 24 (2023) 2978–2987.

[12]. W. Sckudlarek, M.N. Krmasha, K.S. Al-Rubaie, O. Preti, J.C.G. Milan, C.E. da Costa, Effect of austempering temperature on microstructure and mechanical properties of ductile cast iron modified by niobium, J. Mater. Res. Technol. 12 (2021) 2414–2425.

[13]. J.C.K. das Neves, C.M. ˆAngelo, R.M. Souza, A. Sinatora, Effect of mechanically imposed stresses on the contact fatigue resistance of two cast irons with high hardness matrix, Wear 263 (2007) 700–706.

[14]. C. Liu, Y. Du, X. Wang, Q. Zheng, X. Zhu, D. Zhang, D. Liu, C. Yang, B. Jiang, Comparison of the tribological behavior of quench-tempered ductile iron and austempered ductile iron with similar hardness, Wear, 520- 521 (2023), 204668.

[15]. P. Tonolini, L. Montesano, A. Pola, G. Bontempi, M. Gelfi, Wear Behavior of Nb Alloyed Gray Cast Iron for Automotive Brake Disc Application, Metals 13 (2023) 365.

[16]. M. Hussein, M. Ahmed, M. Soliman, L. Z Mohamed, H. Palkowski, R.M. Rashad, A. Nofal, Influence of Austenite Stability on the Machinability of Different Grades of Austempered Ductile Iron (ADI) During Dry Turning Machining, International Journal of Metalcasting, 18(1) (2024) 744–758.

[17]. N. Catipovic, I. Peko, K. Grgic, K. Periša, Multi Response Modelling and Optimisation of Copper Content and Heat Treatment Parameters of ADI Alloys by Combined Regression Grey-Fuzzy Approach, Metals. 14 (2024), 735.

[18]. S. Liu, L. Liang, Research Progress on Alloying of High Chromium Cast Iron—Austenite Stabilizing Elements and Modifying Elements, Crystals, 15 (2025) 210.

[19]. M.Y. Abdellah, H. Alharthi, R. Alfattani, D.K. Suker, H.M. Abu El-Ainin, A.F. Mohamed, M.K. Hassan, A.H. Backar, Mechanical Properties and Fracture Toughness Prediction of Ductile Cast Iron under Thermomechanical Treatment. Metals. 14 (2024), 352.

[20]. C. Chu, W. Chen, Z. Fu, L. Huang, H. Wang, D. Zhu, Realizing good combinations of strength-ductility and corrosion resistance in a Co-free Fe4Ni4Mn2CrTi high-entropy alloy via tailoring Ni/Ti-rich precipitates and heterogeneous structure, Materials Science and Engineering: A, 878 (2023) 145223.

[21]. N. Catipovic, M. Rogante, H. Avdušinovic, K. Grgic, Influence of a Novel Double Tempering Process on the Microstructure and Mechanical Properties of Cu-Alloyed Austempered Ductile Iron with Possible Nano (Micro)-Characterization Using Neutron Beam Techniques. Crystals, 13 (2023), 1359.

[22]. R. Bendikiene, A. Ciuplys, R. Cesnavicius, A. Jutas, A. Bahdanovich, D. Marmysh, A. Nasan, L. Shemet, S. Sherbakov, Influence of Austempering Temperatures on the Microstructure and Mechanical Properties of Austempered Ductile Cast Iron. Metals, 11 (2021), 967.

[23]. O.J. Akinribide, O.D. Ogundare, O.M. Oluwafemi, K. Ebisike, A.K. Nageri, S.O. Akinwamide, F. Gamaoun, P.A. Olubambi, A. Review on Heat Treatment of Cast Iron: Phase Evolution and Mechanical Characterization. Materials. 15 (2022), 7109.

[24]. T. Chen, L. Sun, T. Zhang, C. Liu, X. Cheng, X. Li, In-situ observation and kinetics study on shrinkage defect corrosion of ductile iron in NaCl solution, Corrosion Science 232 (2024) 112034.

[25]. K. Ukoba, O.J. Akinribide, O. Adeleke, S.O. Akinwamide, T-C.n Jen, P.A. Olubambi, Structural integrity and hybrid ANFIS-PSO modeling of the corrosion rate of ductile irons in different environments, Kuwait Journal of Science 51 (2024) 100234.

[26]. P.A. Ramos, I.N.R. Melo, V.H.M. Medeiros, P.P. Brito, Influence of heat treatment time on microstructure evolution of austempered nodular cast iron evaluated by image segmentation, Journal of Alloys and Metallurgical Systems, 8 (2024) 100135.

[27]. B. Wang, G.C. Barber, C. Tao, X. Han, X. Sun, Tribological Performance of Austempered and Tempered Ductile Iron, Metallurgical and Materials Transactions B, 49, (2018) 261–2269.

[28]. M. Landesberger, R. Koos, M. Hofmann, X. Li, T. Boll, W. Petry, W. Volk, Phase Transition Kinetics in Austempered Ductile Iron (ADI) with Regard to Mo Content. Materials. 13 (2020), 5266.

[29]. E. Tyrała, M. Górny, M. Kawalec, A. Muszynska, H.F. Lopez, Evaluation of Volume Fraction of Austenite in Austempering Process of Austempered Ductile Iron. Metals. 9 (2019), 893.

[30]. A.T. Jakubus, M.S. Soiński, P.M. Grzegorz, S.G. Stradomski, Regression Analysis and Optimum Values of Austempering Affecting Mechanical Properties of Compacted Graphite Iron, Materials, 17(20) (2024) 5024.

[31]. J. Bai, H. Xu, Y. Wang, X. Chen, X. Zhang, W. Cao, Y. Xu, Microstructures and Mechanical Properties of Ductile Cast Iron with Different Crystallizer Inner Diameters. Crystals. 12 (2022), 413.

[32]. C.-H. Hsu, C-Y. Lin, W-S. You, Microstructure and Dry/Wet Tribological Behaviors of 1% Cu-Alloyed Austempered Ductile Iron. Materials. 16 (2023), 2284.

[33]. A. Sharma, K.K. Singh, G.K. Gupta, Study on the Effects of Austempering Variables and Copper Addition on Mechanical Properties of Austempered Ductile Iron. In Proceedings of the 6th International & 27th All India Manufacturing Technology, Design and Research Conference (AIMTDR-2016), Pune, India, 16–18 December 2016.

[34]. F.E. Mariani, A.N. Lombardi, L.C. Casteletti, Tribological Evaluation of NbC and VC Layers Produced by Thermo-Reactive Diffusion Treatment in Ductile Cast Irons with Varying Composition, Journal of Materials Engineering and Performance, 32, (2023):5421–5434.

[35]. F.E. Mariani, C. Soares, A.L. Neto, G.E. Totten, L.C. Casteletti, Boro-Austempering Treatment of Ductile Cast Irons, Mater. Res., 2018.

[36]. D.A. Colombo, R.C. Dommarco, A.D. Basso, Rolling Contact Fatigue Behavior of Dual-Phase Austempered Ductile Iron, Wear, 418–419 (2019), 208–214.

[37]. B. Wang, G.C. Barber, F. Qiu, Q. Zou, H. Yang, A Review: Phase Transformation and Wear Mechanisms of Single-Step and Dual-Step Austempered Ductile Irons, J. Mater. Res. Technol., 9(1) 2020, 1054–1069.

[38]. G. Angella, D. Ripamonti, M. Gorny, Comparison Between Ductility Examination and a New Approach Based on Strain Hardening Analysis to Support the Determination of Proper Austempering Times, Int. J. Cast Met. Res., 2020.

[39]. E. Wen, R. Song, W. Xiong, Effect of tempering temperature on microstructures and wear behavior of a 500 HB grade wear-resistant steel. Metals. 9 (2019) 45.

[40]. X. Yan, J. Hu, L. Wang, Z. Chai, W. Sun, W. Xu, The coupled effect of thermal and mechanical stabilities of austenite on the wear resistance in a 0.2C–5Mn-1.6Si steel down to cryogenic temperatures. Wear. 486-487 (2021) 204116.

[41]. S.W. Xia, P. Zuo, Y. Zeng, X. Wu, Influence of nickel on secondary hardening of a modified AISI H13 hot work die steel. Mater Werkst. 50 (2019) 197–203.

[42]. G.W. Ronnie, T. Athanasiops, G. Alexander, The influence of tempering and annealing on the microstructure and sliding wear response of G350 grey cast iron. Wear. 496-497 (2022) 204283.
[43]. S. Wu, D. Wang, X. Tao, X. Wang, R. Zhang, Z. Zhou, S. Zhang, C. Wu, X. Sun, Y. Zhou, C. Cui, Tempering temperature dependence on the microstructure, mechanical properties and wear behaviour of a novel high chromium cast iron, Tribology International 197 (2024) 109831.
[44]. X. Chen, L. Zhao, W. Zhang, H. Mohrbacher, W. Wang, A. Guo, A. Guo, Q. Zhai, Effects of niobium alloying on microstructure, toughness and wear resistance of austempered ductile iron. Mater Sci Eng: A. 760 (2019) 186–94.
[45]. I.C. Turu, R. Gecu, Wear and corrosion behavior of vanadium-alloyed nodular cast irons fabricated by sand-casting. Wear 2023;534-535:205143.
[46]. A.S. Kandemir, R. Gecu, Influence of vanadium content and cooling rate on the characteristics of vanadium-alloyed spheroidal graphite cast irons. J Alloy Compd 2023; 934: 168017.
[47]. X. Chen, L. Zhao, W. Zhang, H. Mohrbacher, W. Wang, A. Guo, Q. Zhai, Effects of niobium alloying on microstructure, toughness and wear resistance of austempered ductile iron. Mater. Sci. Eng. A 2019, 760, 186–194.
[48]. O.J. Akinribide, O.D. Ogundare, O.M. Oluwafemi, K. Ebisike, A.K. Nageri, S.O. Akinwamide, F. Gamaoun, P.A. Olubambi, A Review on Heat Treatment of Cast Iron: Phase Evolution and Mechanical Characterization, Materials 2022, 15, 7109.
[49]. G.A. Gaber, L.Z. Mohamed, H.A. Aly, S. Hosny, Corrosion potential and theoretical studies of fabricated Schiff base for carbidic austempered ductile iron in 1M H2SO4 solution, BMC Chemistry, 18 (2024) 170.
[50]. K. Hayrynen, K. Brandenberg, Carbidic austempered ductile iron (CADI)- the new wear material″, Trans. AFS, 111 (03-088) (2003) 845-850.
[51]. A. Abdelfatah, L.Z. Mohamed, S. El-Hadad, M.E. Moussa, G.A. Gaber, Comprehensive investigation of Si additions and nanocomposite inhibitors on microstructure/ corrosion performance of cast AX53 alloy in 3.5 % NaCl solution, Surface Review and Letters, 2024.
[52]. H.A. El-Fattah, H. Elhelw, M.M. El Sowefy, A. Abdelfatah, L.Z. Mohamed, Corrosion Investigation of Carbon Steel in Different Amine-Based CO2 Removal System, International Journal of Electrochemical Science, 19 (3) (2024), 100511.
[53]. R.M. El-Shorbagy, L.Z. Mohamed, A. AbdelFatah, Effect of Chloride Salt Bath on Electrochemical Behavior and Morphology of 304L and 316L Stainless Steels, Egyptian Journal of Chemistry, 68(4) (2025) 343–354.
[54]. A.E. da Silvaa, I.N.R. de Melob, I.P. Pinheiroa, L.R. da Silvaa, Influence of Niobium Addition on Microstructure and Machinability of High Chromium Cast Iron, Materials Research. 24(5) (2021).
[55]. O.J. Akinribide, S.O. Akinwamide, O.O. Ajibola, B.A. Obadele, S.O.O. Olusunle, P.A. Olubambi, Corrosion behavior of ductile and austempered ductile cast iron in 0.01M and 0.05M NaCl Environments, Procedia Manufacturing, 30 (2019) 167-172.
[56]. G. Beniwal, K.K. Saxena, Effect of niobium addition in grey cast iron: A short review, Materials Today: Proceedings. 26(Part 2) (2020) 2337-2343.
[57]. B. Zhang, K. Xu, X. Zheng, X. Yao, Y. Wang, J. Ge, Study of a Hydrogen Inhibition Method with Sodium Tungstate for Wet Aluminum Dust Removal Systems, Coatings, 10(5) (2020) 431.
[58]. M. Filipovic, Z. Kamberovic, M. Korac, M. Gavrilovski, Microstructure and mechanical properties of Fe–Cr–C–Nb white cast irons, Materials & Design, 47 (2023) 41-48.
[59]. B. Lim, K. Kim, H. Chang, H. Park, Y. Kim, The Effect of Tungstate and Ethanolamines Added in Tap Water on Corrosion Inhibition of Ductile Cast Iron Pipe for Nuclear Power Plants, Metals, 2020.
[60]. Y. Penghui, H. Fu, R. Absi, R. Bennacer, M. Darcherif, S. Ma, J. Lin, X. Guo, Microstructure evolution of carbidic austempered ductile iron at different austempering temperatures, J Mater Sci, 56 (2021) 4843–4857.